Published in final edited form as:
Nature. 2014 May 1; 509(7498): 81–85. doi:10.1038/nature13245.

The electrical conductivity during incipient melting in the oceanic low velocity zone

David Sifré[1,2,3], **Emmanuel Gardés**[1,2,3,4], **Malcolm Massuyeau**[1,2,3], **Leila Hashim**[1,2,3], **Saswata Hier-Majumder**[1,2,3,5,6], and **Fabrice Gaillard**[1,2,3]

[1]Université d'Orléans, ISTO, UMR 7327, 45071 Orléans, France

[2]CNRS/INSU, ISTO, UMR 7327, 45071 Orléans, France

[3]BRGM, ISTO, UMR 7327, BP 36009, 45060 Orléans, France

[4]CEA-CNRS-ENSICAEN-Université de Caen Basse Normandie, CIMAP, UMR 6252, BP 5133, 14070 Caen, France

[5]Department of Geology and CSCAMM, University of Maryland, MD 20742, USA

[6]Dept. of Earth Sciences, Royal Holloway University of London Egham, Surrey, UK

Abstract

A low viscosity layer in the upper mantle, the Asthenosphere, is a requirement for plate tectonics[1]. The seismic low velocities and the high electrical conductivities of the Asthenosphere are attributed either to sub-solidus water-related defects in olivine minerals[2-4] or to a few volume percents of partial melt[5-8] but these two interpretations have shortcomings: (1) The amount of H_2O stored in olivine is not expected to be higher than 50 ppm due to partitioning with other mantle phases[9], including pargasite amphibole at moderate temperatures[10], and partial melting at high temperatures[9]; (2) elevated melt volume fractions are impeded by the too cold temperatures prevailing in the Asthenosphere and by the high melt mobility that can lead to gravitational segregation[11,12]. Here we determined the electrical conductivity of CO_2-H_2O-rich melts, typically produced at the onset of mantle melting. Electrical conductivity modestly increases with moderate amounts of H_2O and CO_2 but it dramatically increases as CO_2 content exceeds 6 wt% in the melt. Incipient melts, long-expected to prevail in the asthenosphere[10,13-15], can therefore trigger its high electrical conductivities. Considering depleted and enriched mantle abundances in H_2O and CO_2 and their effect on the petrology of incipient melting, we calculated conductivity profiles across the Asthenosphere for various plate ages. Several electrical discontinuities are predicted and match geophysical observations in a consistent petrological and geochemical framework. In moderately aged plates (>5Ma), incipient melts most likely trigger both the seismic low velocities and the high electrical conductivities in the upper part of the asthenosphere, whereas for young plates[4], where seamount volcanism occurs[6], higher degree of melting is expected.

Authors contributions: F.G. is leading the project and wrote the first draft. All authors equally contributed to the writing. D.S. and F.G. developed the experimental setup and D.S. performed the conductivity measurements. S.H-M contributed to the discussion and provided editorial assistance with manuscript. D.S. and L.H. did figure 1, E.G. and L.H. did figure 2, D.S. did figure 3 and L.H., M.M. did figure 4.

Europe PMC Funders Author Manuscripts

The lithosphere is a chemically depleted and mechanically strong region of the uppermost mantle, overlying the chemically enriched and mechanically weak asthenosphere [1-3,8,16]. Volatile enrichments in the asthenosphere have long been shown to trigger incipient melting[10,13-15] (that is small degree of partial melting due to small amounts of CO_2 and H_2O) in the upper part of the asthenosphere and a link between incipient melting and seismic low velocity zone has also long been suggested[13,15,17]. In this article, we demonstrate that incipient melting of the mantle by the presence of small amounts of CO_2 and H_2O can also trigger high electrical conductivities. We herein assume that the low viscosity layer, the high electrical conductivity layer (ECL) and low seismic velocity layer (LVZ) are coincident, and use the term Asthenosphere for this layer.

The Asthenosphere is characterized by high electrical conductivities[4,5,18] and reduced S-wave velocities[8,16]. While the characteristics of the Asthenosphere are commonly related to water related defects in olivine[2-4], a number of multidisciplinary observations[5-8,10,13,15,17-20] and the discovery of petit spot volcanoes[21] indicate that the Asthenosphere most likely contains partial melt.

Two issues arise when the observed features of the Asthenosphere are attributed to partial melting: (1) a few volume percentages of basaltic melt are generally required to explain high electrical conductivities, which is problematic as melt would unavoidably tend to rise if present at such high amounts[11-12] and (2) the lithosphere-asthenosphere boundary (LAB) occurs at a near constant depth of 50-75 km for both warm/young and cold/ancient lithospheres[4,5,8,16,18], where the temperature may not be sufficiently high to produce such amounts of melt.

However, incipient CO_2-H_2O rich melts, that are stable under the P-T-fO_2 conditions of the Asthenosphere[10,13-15,17,22-23], allow melting in both warm and cold regions of the Asthenosphere[17]. Low temperature carbonatite melts, composed of almost 50% CO_2, are characterized by high electrical conductivities[19], but their stability is restricted to the coldest and driest regions of the Asthenosphere[17]. Increasing temperature or water content changes the composition of the prevailing melts to intermediates between basalts and carbonatites, often described as carbonated basalts[17,22]. Very little is known about the physical properties of such intermediate volatile-rich melts (CO_2 and H_2O). In particular, their electrical properties have never been measured. In order to address the issues regarding onset of partial melting at the LAB, and to permit a test of the incipient melting model suggested by petrological studies[15,17], we performed electrical conductivity measurements on CO_2-H_2O-rich melts.

We developed a new experimental set-up, specifically adapted for liquids with high conductivities (Extended Data Fig. 1). The high performance of this modified 4-wire method, adapted to ½ inches piston cylinders, is discussed in the Methods section and Extended data figures 1, 2 and 3a. Five melts, with CO_2 and H_2O contents ranging from 10 to 48 wt% and 0 to 10 wt%, respectively, were analysed by impedance spectroscopy in the temperature range 900 - 1500°C at a confining pressure of 3 GPa. We tested the reproducibility of the measurements by taking measurements during both cooling and

heating of the samples (Extended Data Fig. 3a) and we verified that decarbonation and dehydration of samples at high temperature did not affect the conductivity results. Figure 1 reports the measured electrical conductivities as a function of reciprocal temperature. For similar water contents, the electrical conductivity of carbonated basalts is higher than that of hydrated basalts and the difference increases with an increase in the CO_2 content of the melt to a maximum of nearly one log unit. The most CO_2-rich melt has conductivities higher than 200 $S.m^{-1}$. We develop a semi-empirical law that takes into account the two parallel conductive processes operating in carbonated basalts: conduction by covalent polymer-like hydrous silicate melts and ionic conduction by carbonate melts[19].

$$\sigma_{\text{model}} = \left(\sigma_0^{H_2O} \times exp\left(\frac{-E_a^{H_2O}}{RT}\right)\right) + \left(\sigma_0^{CO_2} \times exp\left(\frac{-E_a^{CO_2}}{RT}\right)\right) \quad (1)$$

The calculated conductivities using equation 1, as shown in figure 1, reproduce our measurements and those of ref. 7 on CO_2-free hydrated basalts with an average precision of 5% in σ (see Methods). The effect of CO_2 on melt conductivity, predicted by equation 1, is negligible at low CO_2 content, but increases sharply for CO_2 content higher than 6 wt%. Such a change is most likely caused by an abrupt transition in the melt structure and properties from silicate-type to carbonate-type.

We calculate the mantle electrical conductivity for variable amounts of bulk H_2O and CO_2 contents in a partially molten peridotite. We assume that the interconnected melt is equally distributed between grain edge tubules and grain boundary melt films[18,20,24] (see Methods). The conductivity of hydrated olivine was calculated from ref. 25 and equation 1 was used for CO_2-H_2O-bearing melts. We assume that carbon is exclusively soluble in the melt[23] (carbonate units) and computed the partitioning of water between carbonated melt, pargasite, olivine, and peridotite combining ref. 9, 10 and 22. We report results for partially molten peridotite containing only H_2O (Fig. 2a) and both CO_2 and H_2O (Fig. 2b and 2c). In all simulations, partitioning constraints for CO_2 and H_2O between solids and melts impose that (1) CO_2-H_2O-rich melts can only be produced at the onset of mantle partial melting and (2) that small melt fractions always contain far more CO_2 than H_2O (see top axis in Fig. 2). If > 1% melting is attained, the melt volatile contents drop to values that modestly impacts on their electrical conductivity.

The CO_2-free depleted mantle, containing ca. 200 ppm H_2O[26-28], cannot be conductive at temperatures below 1350°C (i.e. $\sigma \geq 0.1$ $S.m^{-1}$), unless it contains more than ~5 vol.% basaltic melts (Fig. 2a). Only unreasonably high temperatures for the LAB (>1450°C) can make the mantle conductive with small amounts of melt (<1 vol%). Moreover, at high melt percentage, water has almost no effect on mantle conductivity, since its content in the melt remains small (i.e. <1 wt% H_2O negligibly affects basalt conductivity). If an enriched mantle is considered (500 ppm H_2O), a reasonably low melt content (1 vol.%) can trigger high conductivity but it still requires high temperature (>1325°C; Extended Data Fig. 4), and the enriched mantle is also CO_2-rich[26-28].

In presence of CO_2, the formation of incipient CO_2-rich melts (<0.5 vol.%) disproportionately increases the effective electrical conductivity of the mantle (Fig. 2b and 2c). For example, in the depleted mantle, containing 200 ppm H_2O and 200 ppm CO_2[26] and fuelling the dominant part of MORBs[27-28], 0.1-0.15 vol.% of melt at 1325°C can explain the high electrical conductivity of the ECL reported in oceanic domains[5,18,29]. The melt is a carbonated basalt, typically containing 15-35 wt% CO_2 and about 2-3 wt% H_2O (Fig. 2b). Remarkably, the enriched mantle[27-28] with 500 ppm H_2O and 500 ppm CO_2 can produce high conductivities at temperature and melt fractions as low as 1050°C and 0.2 vol%. We also notice that incipient melting of the enriched mantle triggers conductivities that are 2.5 times greater than the depleted mantle making variations in electrical conductivity a powerful probe of the chemical enrichment in the upper mantle.

The stability of incipient melts in the upper part of the asthenosphere has long been shown by petrological constraints[13-15], that are not considered in figure 2. The P-T region of incipient melting in peridotite is shown in Extended Data Fig. 5 together with the stability domain of pargasite, that is the main solid host for water in peridotite containing more than 150-200 ppm[10]. We calculate that the presence of pargasite restricts the amount of water to 40-50 ppm in olivine, according to partition coefficient among peridotite minerals[9,10]. Pargasite is however unstable at T>1070°C[10] and its occurrence must be merely considered for the enriched mantle (>200 ppm H_2O). Based on the P-T phase diagram of Extended Data Fig. 5 and considering oceanic geotherms at 23.5, 35 and 70 Ma, we have calculated 1D conductivity profiles illustrating the impact of several petrological discontinuities (Fig. 3). We have considered the depleted mantle (200 ppm H_2O plus CO_2 varying from 100 to 500 ppm) and the enriched mantle (500 ppm H_2O and 500 ppm CO_2). Variable CO_2 contents in the depleted mantle account for the fact that MORBs have degassed their CO_2 and the carbon content of their source is therefore highly uncertain[26-28].

The upper discontinuity (Fig. 3) predicted by our model is the beginning of incipient melting at ~50 km depth for young/warm plates and at ~70 km for colder/older plates. This discontinuity marks the thermodynamic boundary between CO_2-rich melt and CO_2-rich vapour[14]: the melt being stable at greater depth. In the case of an enriched mantle, an additional discontinuity occurs due to the pargasite dehydration melting reaction (producing CO_2-H_2O rich, low SiO_2 melt) that can be shallower than the previously described discontinuity for young plates (ie. 23.5Ma) and deeper for old plates (70 Ma). At 35 Ma, these two discontinuities occur at the same depth (60 km). The lowest discontinuity shown in figure 3 occurs in the depth interval 120-150 km and is described as the region of redox melting[22,23]; that is the boundary separating diamonds from CO_2-rich melts, the melt being stable at shallower depth. Incipient melting, which triggers the conductive region of the asthenosphere, is therefore permitted between the redox melting lower boundary and the decarbonation upper boundary and this agrees well with electromagnetic observations in oceanic domains[4,5,18,22,29], though ref. 29 indicates slightly deeper ranges.

The increase in conductivity in the incipient melting region is major, being half a log-unit for the depleted mantle (200 ppm CO_2) and more than one log-unit for the mantle containing 500 ppm CO_2. High conductivities of 0.1 S/m or more can be reached for CO_2 contents as low as 300 ppm in the case of young plates. Note that the surprising effect of water (Fig. 3),

where incipient melting in a mantle with 500 ppm H_2O and 500 ppm CO_2 induces lower conductivities than in a mantle with 200 ppm H_2O the same amount of CO_2. The imaging of the 23.5 Ma old LAB by ref. 5 at ~50 km depth revealed conductivities of 0.1-0.2 $S.m^{-1}$. These are definitely not explainable by melting of a CO_2-free H_2O-depleted mantle, since too high temperatures and/or too high melt contents are demanded (Fig. 2). They cannot be explained by pargasite dehydration melting in a CO_2-free H_2O-enriched mantle either, as this process cannot produce high enough conductivities (Fig. 3, Extended Data Fig. 4). Once deciphered in a petrological framework, the conductivities of the LAB in ref. 5 can be reached by incipient melting of a mantle containing 400 ppm CO_2 (Fig. 3). We recall that ref. 5 introduced moderate electrical anisotropy in the inversion of their magnetotelluric data whereas we merely discuss here the geometric mean conductivity, which is much less model dependent.

The presence of CO_2-rich melts in the asthenosphere not only better explains the electrical properties of the Asthenosphere, but also explains the weak dependence of the lithosphere thickness on the age of the oceanic crust (Fig. 4). The bottom of the lithosphere in figure 4 marks a seismic discontinuity characterised by a reduction in S-waves velocity of 5 to 15 %[8,16]. This discontinuity cannot be caused by partial melting of a dry or water under-saturated mantle, as this may only occur at higher depths and temperatures[9] (see blue melting curve on Fig. 4). Previously suggested melting reactions such as the dehydration melting of amphibole[10] also fail to reproduce the depth-age relationships of the LAB (Fig. 4). Remarkably, the CO_2+H_2O melting curve[14], which delimits the upper boundary of the incipient melting region already shown in figure 3, ranges from 50 km down to 80 km depths from the youngest to the oldest lithospheres (purple curve in Fig. 4). This correlates pretty well with the bottom of the lithosphere as imaged by the seismic discontinuity. The lower limit of incipient melting, i.e. the redox melting[22,23], matches also well the lower part of the seismic low velocity zone[8] at depth of about 140-180 km. At low pressures, above the incipient melting region, the decarbonation of the melt forms an impermeable layer in which buoyant CO_2-rich melts are frozen into clinopyroxene-rich residue (with pargasite) and CO_2-rich fluids (Fig. 4). Melting is therefore permitted in the Asthenosphere and the melt cannot rise through the LAB because of the existence of this melt-freezing boundary (see Methods). It is only where the mantle is hot enough to suppress the freezing reaction (that is melting does not anymore require CO_2) and where melt fractions are large enough[12] (2-5 vol %) that melts can rise through the LAB. This occurs for young plates (<5Ma), where volcanic seamounts are observed, and this has also been related[6] to the electrical properties of the young LAB[4].

Incipient melting has long been described as a key petrological process operating in the seismic low velocity region marking the upper asthenosphere[13,15,17]. The mantle geochemistry and petrology in this region argues for production of incipient CO_2-enriched melts[9,10,13,15]. We demonstrate that these melts have conductivities of hundreds of S/m, much higher than CO_2-free hydrated melts or hydrated minerals. Our modelling, despite unavoidable simplifications, considers geochemical and petrological constraints and indicates that mantle with small fractions of CO_2-rich melts at 50-150 km reproduces the electrical properties as well as the depth of the LAB pretty well, whereas CO_2-free systems yields too poor or no agreement with geophysical observations. The presence of CO_2-rich

incipient melts in the Asthenosphere has important implications for radiogenic heat production as such melts are enriched in heat-producing elements like K-U-Th[30]. Moreover, the involvement of CO_2-rich incipient melts is also recognized in petrological processes occurring in the continental and in the cratonic LAB[30]. The Asthenosphere - incipient melting association we suggest here can therefore be extended to geodynamic settings other than the oceanic domains. It remains however to be defined how the mechanical strength of the Asthenosphere can be impacted by small amount of CO_2-H_2O-rich melts and how this can be connected to plate motions.

METHODS

Starting materials

(Extended Data Table 1a). Electrical measurements were performed on five mixtures: 2 dry carbonated melts (CO_2=44 -48wt%), 1 hydrous carbonated melt (CO_2 =25.9 wt%; H_2O=10.2 wt%) and 3 hydrous carbonated basalts (CO_2 = 10.39 to 23.32 wt%; H_2O = 4.43 to 9.22 wt.%). Starting materials used to obtain these mixtures were natural dolomite ($MgCa(CO_3)_2$), a natural basalt (popping rock[31]), salt (NaCl), sodium carbonates (Na_2CO_3) and brucite ($Mg(OH)_2$).

Experiments

All experiments were performed at 3 GPa in ½-inches piston cylinders (graphite-Pyrex-talc assemblages), which was connected to a 1260 Solartron Impedance/Gain Phase Analyzer for electrical conductivity measurements. The temperature was measured with a B-type thermocouple localized on sample top ((Extended Data Fig. 1a)). Oxygen fugacity (fO_2) was not controlled during the measurements but the presence of graphite (furnace) and molten carbonates (sample) should imply an oxygen fugacity close to FMQ-2[23].

We have developed a new protocol specifically adapted for electrical conductivity measurements on highly conductive molten materials (Extended Data Fig. 1). The new design employs a pseudo-4-wire configuration, which removes the electrical contribution of the electrical cell itself (Extended Data Fig. 2a). Such a configuration previously adapted at 1 atm[19,32] is necessary for our measurements at pressure.

Cold pressed pellets (5 mm outer diameter) were cored in their centre in order to place an inner Pt electrode (1 mm). A Pt foil surrounding the sample was used as outer electrode. An alumina jacket isolated the entire electrical cell from the graphite furnace. The sample impedance was measured between the two electrodes arranged in a co-axial geometry[33,34]. The inner electrode was connected to the impedance spectrometer via the two wires of the thermocouple[34]. The outer electrode was connected to a nickel cylinder (located 5 mm above the sample) that was mounted in series with two additional wires (B-type thermocouples) (Extended Data Fig. 1a).

Impedance spectra, conductivity calculations and uncertainties

The impedance spectra were collected during heating and cooling cycles (Extended Data Table 2a) at different temperature plateaus in the frequency range 1 Hz to 1 MHz.

Conversely to the spectra collected at low temperatures (i.e. solid samples showing impedance arcs), high temperature spectra (i.e. molten samples) indicated vertical lines (Extended Data Fig. 2b). These spectra correspond to inductance-dominated signals and the intercept of each spectrum with the X-axis yielded the resistance of the sample.

Reproducibility of electrical measurements was validated by performing the measurements during heating and cooling cycles. For the hydrated experiments (HC and HCB-9, -7, -4), a step of about 10 min was operated at 700°C (before brucite dehydration) and temperature was rapidly raised (< 10 sec) to 1300-1410°C (i.e. temperature of molten state), which limited sample dehydration.

Data reductions and uncertainties

The electrical conductivities of the samples were calculated from the measured resistances using the following relationship[33,34]:

$$\sigma = \frac{ln\,(r_{out}/r_{in})}{2\pi hR} \quad (2)$$

with σ being the electrical conductivity in $S.m^{-1}$, r_{out}, r_{in}, h, respectively the outer radius, the inner radius and the height of the samples in m, and R, the resistance of the sample in Ω (Extended Data Fig. 1b and 2b).

Uncertainties in σ were calculated considering geometrical factors of the samples (Extended Data Fig. 1b) and propagated errors of each measured resistance. The uncertainties on σ are 7 % on average for all measurements and reach a maximum of 16% on HCB-4.

Sample characterization

Scanning electron microscope (SEM) imaging and electron microprobe analyses (EMPA) were systematically operated after each experiment. Determination of r_{out}, r_{in} and h by SEM imaging showed an average decrease of 20% compared to the initial geometry, most likely due to porosity loss during melting (Extended Data Fig. 1b). No melt leak was observed and the entire sample remained sandwiched between the MgO plugs and the electrodes.

EMPA were conducted at 15 KeV, 10 nA and 10 sec counting on peak elements. The beam size (100 μm × 100 μm) was adapted to obtain average chemical compositions, smoothing the heterogeneities due to quench crystallizations. Compositions before and after experiments indicates no contamination by the MgO surrounding the sample and no considerable volatile loss from the sample (Extended Data Table 1b). CO_2 content were determined using the by-difference method[22] and indicate negligible decarbonation.

An elemental analyser, type Flash 2000 (Thermo Scientific), was used to measure H_2O content of sample (before and) after experiments. Samples are heated to >1500°C and the released H_2O is reduced into elemental H being finally detected by a highly sensitive thermal conductivity detector. This gives water content with a precision of +/− 0.5 wt%. We observed a negligible dehydration during conductivity measurements.

Conductivity Results

Extended Data Fig. 3a shows the good reproducibility of the electrical measurements during heating and cooling cycles. The conductivity-temperature relationships for each sample were fitted using an Arrhenius law:

$$\sigma = \sigma_0 \times e^{-E_a/RT} \quad (3)$$

with σ, the conductivity of the sample ($S.m^{-1}$), σ_0, the pre-exponential factor ($S.m^{-1}$), E_a the activation energy ($J.mol^{-1}$), R, the gas constant and T, the temperature (K).

Calculated pre-exponential factors and activation energies are presented in Extended Data Table 2b.

Increasing the CO_2 concentration in the melt drastically increases its conductivity. Furthermore, we observed that CO_2 tends to decrease both activation energies and pre-exponential factors.

Conductivity Modelling

The semi-empirical law that we have developed can be considered as the sum of two conductive processes operating in carbonated basalts: (i) conduction in the hydrous silicate melts by interstitial sodium mobility[7,33-34] and (ii) conduction in CO_2-rich melts caused by the motion of all species in ionic liquids[19] (equation 1).

The pre-exponential factor σ_0 and the activation energy E_a for both H_2O and CO_2 terms are related by a compensation law[35,36] (Extended Data Fig. 3b):

$$ln\,\sigma_0^{volatile} = \left(E_A^{volatile} \times d\right) + e \quad (4)$$

the decrease of activation energy as a function of volatile content is exponential:

$$E_A^{volatile} = a \times exp\left(-b \times C^{volatile}\right) + c \quad (5)$$

$C^{volatile}$ is the CO_2 and H_2O content in wt%.

Thus, the set of Eqs 1, 4 and 5 directly relate melt conductivities to melt H_2O and CO_2 contents. We have determined the Arrhenius parameters for the melt composition as a function of H_2O contents using data in ref. 7 in the temperature range 1200-1500°C. a, b, c, d and e parameters for H_2O were obtained by fitting these data with Eqs 4 and 5 (Extended Data Table 3). The best parameters for CO_2 were obtained by minimizing the differences between our measured conductivities and the CO2-free values returned by equation 1 (Extended Data Table 3). In doing so, we assumed that the effect of water on electrical conductivity is similar and modest in both silicate and carbonate melts, which is indeed what our measurements show (see Extended Data Fig. 3a, samples C vs. HC). Our model reproduces the experimental measurements on σ, in S/m, (ours and that of ref. 7) within an average error of 5% (max 10%).

Figures 2 & 3

The bulk rock is considered as a peridotite containing a fraction of interconnected melt, where volatiles partition between the solid and the melt phase. The bulk H_2O content is related to H_2O in melt and in peridotite as:

$$C_{H_2O}^{melt} = \frac{C_{H_2O}^{bulk}}{X_m^{melt} + (1 - X_m^{melt})\, D_{H_2O}^{perid/melt}} \quad \text{and}$$
$$C_{H_2O}^{perid} = \frac{C_{H_2O}^{bulk} D_{H_2O}^{perid/melt}}{X_m^{melt} + (1 - X_m^{melt})\, D_{H_2O}^{perid/melt}} \qquad (6)$$

where X_m^{melt} is the mass fraction of melt and $D_{H_2O}^{perid/melt}$ is the partition coefficient of H_2O between peridotite and melt (0.007, i.e. average partition coefficient over 1.5-4 GPa[9,37]).

The concentration of H_2O in olivine is:

$$C_{H_2O}^{ol} = C_{H_2O}^{perid} \frac{D_{H_2O}^{ol/melt}}{D_{H_2O}^{perid/melt}} \qquad (7)$$

differs from that of peridotite since $D_{H_2O}^{ol/melt}$ is about 0.002 according to ref. 9. (see also figure 6 of ref.9 for modal proportion of mineral phases in peridotite $Ol_{58}Opx_{28}Cpx_{12}Spn_2$).

Pargasite amphibole was considered to affect the distribution of water for bulk water content exceeding 200 ppm (enriched mantle in Fig. 2c, Fig. 3 and Extended Data Fig. 4). We computed that the water content exceeding 200 ppm bulk goes in pargasite and computed the partitioning of water among NAMs following ref. 9. If temperatures exceed ca. 1070°C (see Extended Data Fig. 5), then pargasite dehydration melting occurs and water partitions between melt and the solids as described above.

CO_2 distributes exclusively in the liquid phase[23,38], i.e. $D_{CO_2}^{perid/melt} = 0$. Therefore:

$$C_{CO_2}^{melt} = \frac{C_{CO_2}^{bulk}}{X_m^{melt}} \quad \text{and} \quad C_{CO_2}^{perid} = 0 \qquad (8)$$

At small melt fractions, this can lead to CO_2 concentrations higher than that of carbonate (>~45 wt. %) or, in other words, to CO_2 saturation; Calculations performed in saturated- ranges are mentioned in Fig. 2b and 2c.

Conversion from mass to volume fraction of melt is done considering volume properties of silicate melts[39] and carbonate melts[40,41]:

$$X_\nu^{melt} = \left(1 + \left(\frac{1}{X_m^{melt}} - 1\right) \frac{d_{melt}}{d_{perid}}\right)^{-1} \qquad (9)$$

where d_{perid} is the density of peridotite, i.e. 3.3, and d_{melt} is the density of melt. As there are no data for the density of hydrous carbonated basalts, we estimate the density of these melts using a simple mixing law:

$$d_{melt} = \frac{C_{H_2O}^{melt}}{100} d_{H_2O} + \frac{C_{carb}^{melt}}{100} d_{carb} + \left(1 - \frac{C_{H_2O}^{melt} + C_{carb}^{melt}}{100}\right) d_{basalt} \quad (10)$$

where concentrations are expressed as wt. % d_{H_2O} = 1.4 (considering 12 cc/mol for H_2O partial volume in melts). The mass percent of carbonate (M-CO_3, where M denotes cations such as Ca, Mg and others) in melt C_{carb}^{melt} is approximated as $2 \times C_{CO_2}^{melt}$. Carbonate density d_{carb} was set to 2.4 according to the density of molten carbonates at 1 bar[40]. The use of CO_2 partial molar volume calculated in ref. 41 yields similar density results. The density of d_{basalt} was taken as 2.8 (ref. 39).

The conductivity of the melt $\sigma_{melt}\left(C_{H_2O}^{melt}, C_{CO_2}^{melt}, T\right)$ was calculated using equation 1. The conductivity of the peridotite was assumed to be controlled by that of hydrous olivine[25].

The bulk conductivity was calculated using the mean of tube[42-44]:

$$\sigma_{tube} = \frac{1}{3} X_v^{melt} \sigma_{melt} + \left(1 - X_v^{melt}\right) \sigma_{ol} \quad (11)$$

and film[44-47]:

$$\sigma_{layer} = \frac{\left[\left(1 - X_v^{melt}\right)^{2/3} - 1\right] \sigma_{melt} - \left(1 - X_v^{melt}\right)^{1/3} \sigma_{ol}}{\left[1 - X_v^{melt} - \left(1 - X_v^{melt}\right)^{2/3}\right] \sigma_{melt} + \left[\left(1 - X_v^{melt}\right)^{2/3} - \left(1 - X_v^{melt}\right) - 1\right] \sigma_{ol}} \sigma_{melt} \quad (12)$$

Geometries resulting in values almost similar to refs 20 and 46. Remarkably, our system is rather insensitive to melt geometry since the difference between both laws is mostly lower than 0.2 log units. We therefore averaged the two laws:

$$\sigma_{bulk}\left(X_v^{melt}, C_{H_2O}^{bulk}, C_{CO_2}^{bulk}, T\right) = \frac{\sigma_{tube} + \sigma_{layer}}{2}. \quad (13)$$

The bulk conductivity of partially molten peridotite reported in Fig. 2 and 3 as well as in the text was calculated using this last equation (13).

Melt fraction in Fig. 3 was approximated as $X_m^{melt} = 2.5 \times {CO_2}^{bulk} + 6 \times {H_2O}^{bulk}$ (Extended Data Fig. 6).

Buoyant basalts versus incipient melts

An impermeable layer has been suggested to prevent the melt prevailing in the LAB from rising to the surface[49]. The rate of melt ascent due to buoyancy is otherwise expected to be of the order of several cm/year[11,12], if melt content is 3-5 vol. %. Our model of incipient

melting implies an impermeable boundary that is caused by phase relationships[14], i.e. a thermodynamic boundary through which melt cannot rise. We furthermore emphasise the limited melt mobility[50] at the small melt fraction of interest as, in particular, surface tensions would unavoidably tend to retain the buoyant melt[51]. To conclude, if basalts, being anyway not thermodynamically stable in the asthenosphere, tend to migrate out of the asthenosphere[52], small melt fractions may in contrast be mechanically stable in the LAB.

Supplementary Material

Refer to Web version on PubMed Central for supplementary material.

Acknowledgments

This work, part of the ElectroLith project, benefited from funding by the European Research Council (ERC project #279790) and the French agency for research (ANR project # 2010 BLAN62101). SH-M acknowledges support from the NSF grant EAR1215800 and a grant from the University of Orleans.

REFERENCES

1. Höink T, Jellinek AM, Lenardic A. Viscous coupling at the lithosphere-asthenosphere boundary. Geochem.Geophys. Geosyst. 2011; 12:Q0AK02.
2. Hirth G, Kohlstedt DL. Water in the oceanic upper mantle: Implications for rheology, melt extraction and the evolution of the lithosphere. Earth Planet. Sci. Lett. 1996; 144:93–108.
3. Karato S. On the origin of the asthenosphere. Earth Planet. Sci. Lett. 2012; 321:95–103.
4. Evans RL, Hirth G, Baba K, Forsyth D, Chave A, Mackie R. Geophysical evidence from the MELT area for compositional controls on oceanic plates. Nature. 2005; 437:249–252. [PubMed: 16148932]
5. Naif S, Key K, Constable S, Evans RL. Melt-rich channel observed at the lithosphere-asthenosphere boundary. Nature. 2013; 495:356–359. [PubMed: 23518564]
6. Caricchi L, Gaillard F, Mecklenburgh J, Le Trong E. Experimental determination of electrical conductivity during deformation of melt-bearing olivine aggregates: Implications for electrical anisotropy in the oceanic low velocity zone. Earth Planet. Sci. Lett. 2011; 302:81–94.
7. Ni H, Keppler H, Behrens H. Electrical conductivity of hydrous basaltic melts: implications for partial melting in the upper mantle. Contrib. Mineral. Petrol. 2011; 162:637–650.
8. Schmerr N. The Gutenberg discontinuity: melt at the lithosphere-asthenosphere boundary. Science. 2012; 335:1480–1483. [PubMed: 22442480]
9. Hirschmann M, Tenner T, Aubaud C, Withers AC. Dehydration melting of nominally anhydrous mantle: The primacy of partitioning. Phys. Earth Planet. Inter. 2009; 176:54–68.
10. Green DH, Hibberson WO, Kovács I, Rosenthal A. Water and its influence on the lithosphere-asthenosphere boundary. Nature. 2010; 467:448–U97. [PubMed: 20865000]
11. Hier-majumder S, Courtier A. Seismic signature of small melt fraction atop the transition zone. Earth Planet. Sci. Lett. 2011; 308:334–342. doi: 10.1016/j.epsl.2011.05.055.
12. Faul UH. Melt retention and segregation beneath mid-ocean ridges. Nature. 2001; 410:920–3. doi: 10.1038/35073556. [PubMed: 11309614]
13. Presnall DC, Gudfinnsson GH. Carbonate-rich melts in the oceanic low-velocity zone and deep mantle. Geol. Society of America. 2005; 388:207–216. Special Papers.
14. Wallace ME, Green DH. An experimental determination of primary carbonatite magma composition. Nature. 1988; 335:343–346.
15. Green DH, Liebermann RC, Phase-equilibra and elastic properties of a pyrolite model for oceanic upper mantle. Tectonophysics. 1976; 32:61–92.
16. Fischer KM, Ford HA, Abt DL, Rychert CA. The Lithosphere-Asthenosphere Boundary. Annual Review of Earth and Planetary Sciences. 2010; 38:551–575.

17. Hirschmann MM. Partial melt in the oceanic low velocity zone. Phys. Earth Planet. Inter. 2010; 179:60–71.
18. Utada H, Baba K. Estimating the electrical conductivity of the melt phase of a partially molten asthenosphere from seafloor magnetotelluric sounding data. Physics of the Earth and Planetary Interiors. 2013http://dx.doi.org/10.1016/j.pepi.2013.12.004
19. Gaillard F, Malki M, Iacono-Marziano G, Pichavant M, Scaillet B. Carbonatite melts and electrical conductivity in the asthenosphere. Science. 2008; 322:1363–1365. [PubMed: 19039132]
20. Yoshino T, Laumonier M, McIsaac E, Katsura T. Electrical conductivity of basaltic and carbonatite melt-bearing peridotites at high pressures: Implications for melt distribution and melt fraction in the upper mantle. Earth Planet. Sci. Lett. 2010; 295:593–602.
21. Hirano N, Takahashi E, Yamamoto J, et al. Volcanism in Response to Plate Flexure. Science. 2006; 313:1426–1428. [PubMed: 16873612]
22. Dasgupta R, Mallik A, Tsuno K, Withers AC, Hirth G, Hirschmann MM. Carbon-dioxide-rich silicate melt in the Earth's upper mantle. Nature. 2013; 493:211–U222. [PubMed: 23302861]
23. Stagno V, Ojwang DO, McCammon CA, Frost DJ. The oxidation state of the mantle and the extraction of carbon from Earth's interior. Nature. 2013; 493:84. [PubMed: 23282365]
24. Minarik WG, Watson EB. Interconnectivity of carbonate melt at low melt fraction. Earth Planet. Sci. Lett. 1995; 133:423–437.
25. Jones AG, Fullea J, Evans RL, Muller MR. Water in cratonic lithosphere: Calibrating laboratory determined models of electrical conductivity of mantle minerals using geophysical and petrological observations. Geochem. Geophys. Geosyst. 2012; 13:Q06010.
26. Cartigny P, Pineau F, Aubaud C, Javoy M. Towards a consistent mantle carbon flux estimate: Insights from volatile systematics (H2O/Ce, δD, CO2/Nb) in the North Atlantic mantle (14° N and 34° N). Earth Planet. Sci. Lett. 2008; 265:672–685.
27. Marty B. The origins and concentrations of water, carbon, nitrogen and noble gases on Earth. Earth Planet. Sci. Lett. 2012; 313-314:56–66.
28. Dasgupta R, Hirschmann MM. The deep carbon cycle and melting in Earth's interior. Earth Planet. Sci. Lett. 2010; 298:1–13.
29. Lizarralde D, Chave A, Hirth G, Schultz A. Northeastern Pacific mantle conductivity profile from long-period magnetotelluric sounding using Hawaii-to-California submarine cable data. J. Geophys. Res. 1995; 100(B9):17837–17854.
30. O'Reilly SY, Griffin WL. The continental lithosphere-asthenosphere boundary: Can we sample it? Lithos. 2010; 120:1–13.
31. Javoy M, Pineau F. The volatiles record of a "popping" rock from the Mid-Atlantic Ridge at 14 ° N: chemical and isotopic composition of gas trapped in the vesicles. Earth Planet. Sci. Lett. 1991; 107:598–611.
32. Pommier A, Gaillard F, Malki M, Pichavant M. Methodological re-evaluation of the electrical conductivity of silicate melts. Am. Mineral. 2010; 95:284–291.
33. Gaillard F. Laboratory measurements of electrical conductivity of hydrous and dry silicic melts under pressure. Earth Planet. Sci. Lett. 2004; 218:215–228.
34. Hashim L, Gaillard F, Champallier R, Le Breton N, Arbaret L, Scaillet B. Experimental assessment of the relationships between electrical resistivity, crustal melting and strain localization beneath the Himalayan-Tibetan belt. Earth Planet. Sci. Lett. 2013; 373:20–30. doi: 10.1016/j.epsl.2013.04.026.
35. Pommier A, Gaillard F, Pichavant M, Scaillet B. Laboratory measurements of electrical conductivities of hydrous and dry Mount Vesuvius melts under pressure. J. Geophys. Res. Solid Earth. 2008; 113:B05205.
36. Tyburczy J, Waff HS. Electrical conductivity of molten basalt and andesite to 25 kilobars pressure: Geophysical significance and implications for the charge transport and melt structure. J. Geophys. Res. 1983; 88:2413–2430.
37. Katz RF, Spiegelman M, Langmuir CH. A new parameterization of hydrous mantle melting. Geochem. Geophys. Geosyst. 2003; 4(9):1073. doi: 10.1029/2002GC000433.
38. Keppler H, Wiedenbeck M, Shcheka SS. Carbon solubility in olivine and the mode of carbon storage in the Earth's mantle. Nature. 2003; 424:414–416. [PubMed: 12879066]

39. Lange RA, Carmichael ISE. Thermodynamic properties of silicate liquids with emphasis on density thermal expansion and compressibility. Rev. Mineral. 1990; 24:25–64.
40. Liu Q, Lange RA. New density measurements on carbonate liquids and the partial molar volume of the CaCO3 component. Contrib. Mineral. Petrol. 2003; 146:370–381.
41. Guilllot B, Sator N. Carbon dioxide in silicate melts: A molecular dynamics simulation study. Geoch. Cosmoch. Acta. 2011; 75:1829–1857.
42. ten Grotenhuis SM, Drury MR, Spiers CJ, Peach CJ. Melt distribution in olivine rocks based on electrical conductivity measurements. J. Geophys. Res. 2005; 110:B12201.
43. Hammouda T, Laporte D. Ultrafast mantle impregnation by carbonatite melts. Geology. 2000; 28:283–285.
44. Glover PWJ, Hole MJ, Pous J. A modified Archie's law for two-conducting phases. Earth Planet. Sci. Lett. 2000; 180:369–383.
45. Partzsch GM, Schilling FR, Arndt J. The influence of partial melting on the electrical behaviour of crustal rocks: laboratory examinations, model calculations and geological interpretations. Tectonophysics. 2000; 317:189–203.
46. Yoshino T, McIsaac E, Laumonier M, Katsura T. Electrical conductivity of partial molten carbonate peridotite. Phys. Earth Planet. Inter. 2012; 194:1–9.
47. Garapić G, Faul UH, Brisson E. High-resolution imaging of the melt distribution in partially molten upper mantle rocks: evidence for wetted two-grain boundaries. Geochem. Geophys. Geosyst. 2013; 14:556–566.
48. Green DH, Falloon TJ. Primary magmas at mid-ocean ridges, "hotspots," and other intraplate settings: Constraints on mantle potential temperature. Geol. Society of America. 2005; 388:217–247. Special Papers. doi: 10.1130/0-8137-2388-4.217.
49. Katz RF, Weatherley SM. Consequences of mantle heterogeneity for melt extraction at mid-ocean ridges. Earth Planet. Sci. Lett. 2012; 335-336:226–237.
50. Hier-Majumder S, Ricard Y, Bercovici D. Role of grain boundaries in magma migration and storage. Earth Planet. Sci. Lett. 2006; 248:735–749.
51. Takei Y, Holtzman BK. Viscous constitutive relations of solid-liquid composites in terms of grain boundary contiguity: 1. Grain boundary diffusion control model. J. Geophys. Res. 2009; 114:B06205.http://dx.doi.org/10.1029/2008JB005850
52. Sakamaki T, Suzuki A, Ohtani E, Terasaki H, Urakawa S, Katayama Y, Funakoshi K-I, Wang Y, Hernlund JW, Ballmer MD. Ponded melt at the boundary between the lithosphere and asthenosphere. Nature Geosciences. 2013; 6:1041–1044. doi: 10.1038/ngeo1982.
53. Hirschmann MM. Mantle solidus: Experimental constraints and the effects of peridotite composition. Geochem. Geophys. Geosystems. 2000; 1
54. Dasgupta R. Ingassing, storage, and outgassing of terrestrial carbon through geologic time. Reviews in Mineral. Geoch. 2013; 75:183–229.
55. Iacono-Marziano G, Morizet Y, Le Trong E, Gaillard F. New experimental data and semi-empirical parameterization of H2O-CO2 solubility in mafic melts. Geoch. Cosmosch. Acta. 2012; 97:1–23.

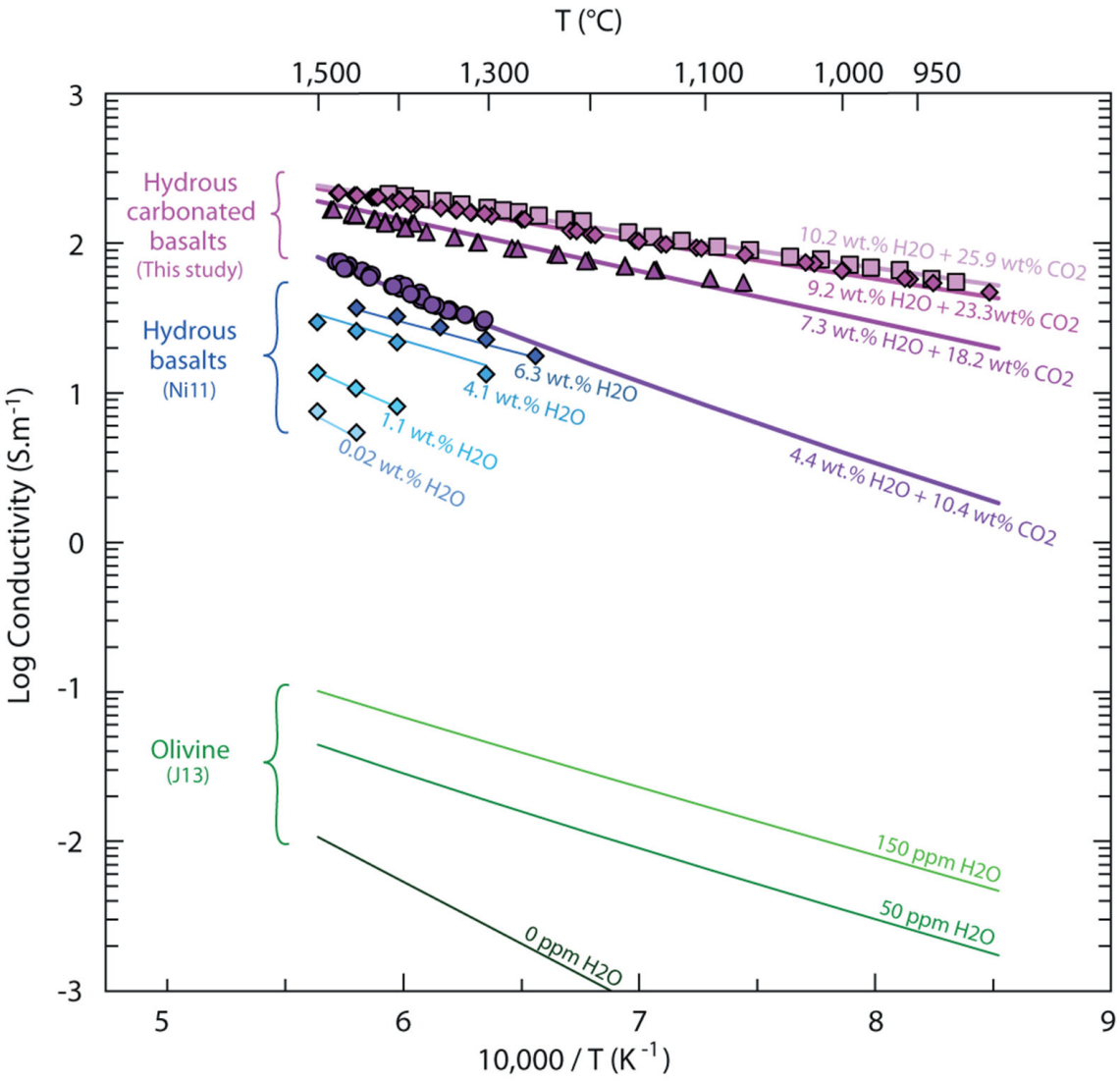

Figure 1. Electrical conductivity of hydrous carbonated basalts vs. hydrated basalts and hydrous olivine

The conductivities of the hydrous carbonated basalts experimentally measured in this study are by far the highest, reaching up to 200 S/m and being about one and four order of magnitude higher than hydrated basalts[7] and hydrous olivine[25], respectively. The fitting curves are calculated according to our conductivity model for CO_2- and H_2O-bearing melts (Eq. 1).

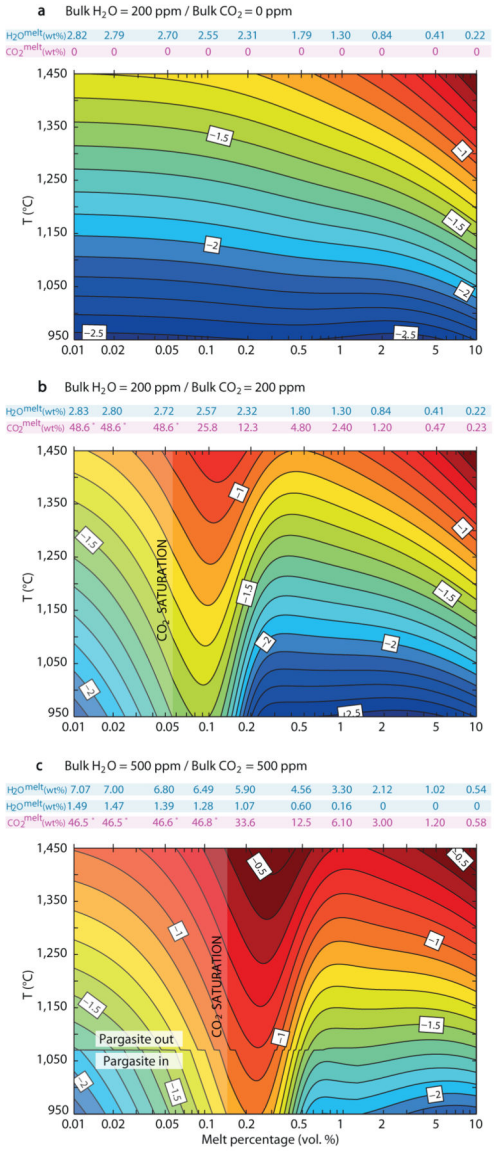

Figure 2. The incipient melt effect on the electrical conductivity of depleted and enriched carbonated peridotites

The conductivity of partially molten peridotite (log values increasing from cold to warm colours) is reported as a function of melt content and temperature for **a,** CO_2-free peridotite with 200 ppm H_2O and **b, c,** depleted and enriched CO_2-bearing hydrous systems. H_2O partitions between minerals and melt, and CO_2 distributes in melt only (Methods). Addition of CO_2 triggers a peak in conductivity at 0.1-0.3 vol.% of melt, where the intergranular liquid is CO_2-rich and therefore highly conductive. At higher degrees of melting, the bulk conductivity decreases since volatiles are diluted in the melt (melt H_2O and CO_2 are tabulated atop each panel), which becomes basaltic. A peridotite with 0.1 vol.% carbonated basalt is as conductive as with 10 vol.% basalt. Two sets of melt H_2O contents are given for the bottom panel (500 ppm H_2O and CO_2), which correspond to pargasite-saturated (low T<1070°C, italics) and paragsite-undersaturated (T>1070°C, normal) melt water contents.

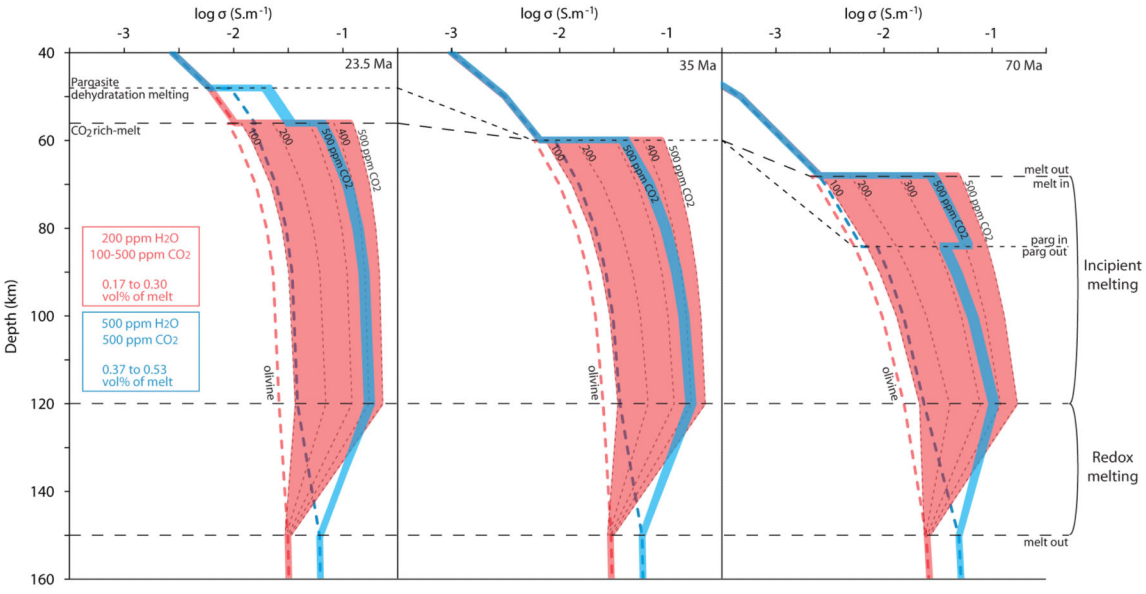

Figure 3. Petrologically-based conductivity profiles across the incipient melting region under the lithosphere-asthenosphere boundary for various ages

Top axis indicates electrical conductivity and how it varies with depth during cooling of the lithosphere for ages of 23.5, 35 and 70 Ma (see choices of geotherm in Fig. 4). Conductivities were calculated according to the same model used in Fig. 2 (Methods). Several electrical discontinuities are predicted at variable depths based on the phase-equilibria relationships shown in Extended Data Fig. 5-6; the most striking conductivity jumps is related to the upper and lower boundaries of incipient melting (55-150 km). The volatile depleted and enriched mantles are considered and one can appreciate that the conductivity during incipient melting is strongly correlated to CO_2 contents (grey dashed lines labelled from 100 to 500 ppm).

Europe PMC Funders Author Manuscripts

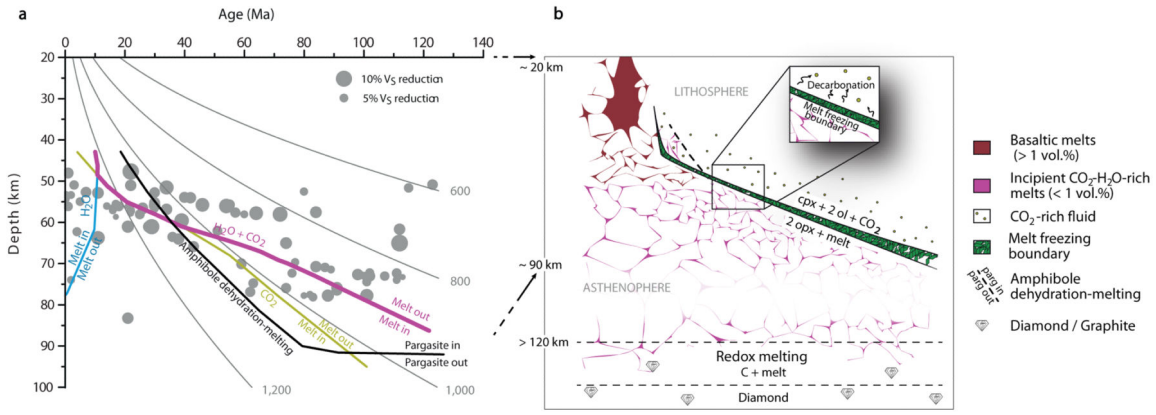

Figure 4. The oceanic seismic low velocity zone bracketed by the upper and lower boundary of incipient melting

a, Oceanic crustal ages versus depth of seismic discontinuities (Vs reductions) marking the LAB (grey circles[8]) beneath the Pacific Ocean. Colour curves designate the solidi for hydrated (200 ppm H_2O; blue), carbonated (green) and H_2O-undersaturated carbonated (purple) peridotites. Isotherms (grey curves) are calculated from a half-space sudden cooling model, assuming[8] $\Delta T = 1350°C$, an average plate velocity of 8 cm•yr^{-1} and a thermal diffusivity of 1 mm^2•s^{-1}. Varying the plate velocity does not change the plot. **b,** A visual picture capturing the domain of incipient melting in the oceanic low velocity zone. The LVZ is lower-bounded by the redox melting[22,23] and upper-bounded by the decarbonation[14] leading to the freezing of incipient melts. This boundary constitutes an impermeable layer leaving a clinopyroxene-rich residue and a CO_2-rich vapour phase.

Europe PMC Funders Author Manuscripts